A new observational solar irradiance composite

Margit Haberreiter[1], Micha Schöll[1,2], Thierry Dudok de Wit[2], Matthieu Kretzschmar[2], Stergios Misios[3,4], Klairie Tourpali[3], and Werner Schmutz[1]

Abstract. Variations in the solar spectral irradiance (SSI) are an important driver of the chemistry, temperature, and dynamics of the Earth's atmosphere, and ultimately the Earth's climate. To investigate the detailed response of the Earth's atmosphere to SSI variations, a reliable SSI dataset is needed. We present an observational SSI composite dataset **that is based on 20 instruments, and has been built by using probabilistic approach** that takes into account the scale-dependent uncertainty of each available SSI observation. We compare the variability of this new composite with available SSI reconstructions and discuss the respective modelled responses in the Earth's atmosphere. As the composite is based on purely statistical means we consider it as a valuable independent dataset.

1. Introduction

The impact of solar variability on the Earth's climate has a long history as a research field, and has also become a hotly debated topic [*Haigh*, 1994; *Haigh et al.*, 2010; *Ermolli et al.*, 2013; *Ball et al.*, 2016]. This impact is mediated by several mechanisms including direct solar heating of the Earth's surface, changes in stratospheric ozone, and the impact of energetic particles [*Haigh*, 2007; *Gray et al.*, 2010; *Ermolli et al.*, 2013; *Solanki et al.*, 2013].

Although there is strong evidence for this natural forcing to be weak in comparison to that of man-made greenhouse gases, large uncertainties remain regarding the magnitude of the impacts, and the mechanisms involved [*Stocker and Qin*, 2014]. Two key mechanisms have been identified and investigated in a number of modelling studies: The first one, known as the *bottom-up* mechanism, involves direct changes in the troposphere, caused by the variability **primarily in the visible part of the solar spectrum,** directly penetrating to the lower troposphere, warming the surface and modulating the atmosphere-ocean interactions [e.g. *Meehl et al.*, 2009]. The second one, named *top-down* mechanism, involves the direct influence of solar ultraviolet (UV) variations – in particular below 200 nm – on the upper atmosphere, causing an increase in stratospheric ozone and related warming, and indirect dynamical effects at lower stratospheric levels, and finally influencing surface climate through stratosphere-troposphere coupling [e.g. *Haigh*, 1994; *Matthes et al.*, 2006].

For the *top-down* mechanisms the key input variable is the solar UV radiation, on which this paper will concentrate. Direct observations of the spectrally-resolved solar irradiance (or SSI, for Solar Spectral Irradiance) started in the 1970s. These observations however, are fragmented in time and in wavelength. Only in 2003 - with the launch of the SORCE spacecraft - did the continuous monitoring of the solar spectrum really start. As a consequence, our present knowledge of the solar variability in different parts of the spectrum is limited. However, a continuous SSI dataset is crucially needed to assess decadal, and multi-decadal time scales that are most relevant for climate studies. This paucity of observations is further complicated by numerous problems; making radiometrically accurate SSI observations is notoriously challenging, as instruments degrade in time, have a limited lifetime, and rarely allow in-flight calibration.

To overcome these problems, and reconstruct the SSI over longer periods, several SSI models have been developed and their output, the reconstructed SSI time series, has been widely used to represent solar spectral variations in climate and chemistry-climate modelling studies [*Matthes et al.*, 2006; *Austin et al.*, 2008; *Ermolli et al.*, 2013; *Solanki et al.*, 2013; *Hood et al.*, 2015; *Mitchell et al.*, 2015; *Misios et al.*, 2015].

However, and while most of them correctly reproduce recent SSI observations, large uncertainties remain regarding their ability to reconstruct past variations on multi-decadal time scales. More importantly, all these models are eventually trained and tested on the few available SSI observations. This situation has led to the international collaborative project **SOLID (First European Comprehensive Solar Irradiance Data Exploitation, http://projects.pmodwrc.ch/solid/)** with the aim of collecting and merging all available SSI observations into one single composite that will finally offer better conditions for training SSI models, understanding solar variability, and assessing its impact on climate. Such homogeneous datasets are of particular importance for initiatives such as the Climate Model Intercomparison Project (CMIP, http://www-pcmdi.llnl.gov/projects/cmip/), which aims at quantifying the contributions of various forcings, including the solar forcing.

Although the SOLID composite addresses the full solar spectrum, including the visible and near-infrared, in this paper we focus on the UV only, from 100 nm to 400 nm because of its key role in Sun-climate studies. Indeed, the visible and near-infrared bands mostly lead to direct heating of the surface and oceans only, and their forcing can be conveniently summarised in the spectrally-integrated SSI, named Total Solar Irradiance (TSI). **The TSI has received considerable attention, and it's reconstruction efforts have a long history** [*Fröhlich and Lean*, 1998; *Kopp and Lean*, 2011]. In comparison, the SSI has received much less attention, while its variability also raises many questions. Recent observations by the SORCE satellite, for example,

[1]Physikalisch-Meteorologisches Observatorium and World Radiation Center, Dorfstrasse 33, CH-7260 Davos Dorf, Switzerland

[2]LPC2E/CNRS and Université d'Orléans, 3 A Av. de la Recherche Scientifique, 45071 Orléans, France

[3]LAP, Aristotle University of Thessaloniki, 54124 Thessaloniki, Greece

[4]Atmospheric, Oceanic and Planetary Physics, Oxford University, Oxford, UK

0148-0227/17/$9.00

have revealed SSI variations in the UV band that depart from past observations, and could potentially lead to a different climate response to the solar cycle [*Haigh et al.*, 2010]. These variations are still hotly debated [*Lean and DeLand*, 2012], and provide yet another motivation for building a single composite that would allow different periods to be compared. Recently, *Ball et al.* [2016] investigated the response of the Earth's atmosphere to different SSI datasets and concluded that the simulated ozone response driven by the SORCE SSI observations cannot be reconciled with ozone observations.

The first attempt to merge different SSI observations in a single UV dataset was made by *DeLand and Cebula* [2008] who created a dataset with daily spectra covering the 120–400 nm wavelength range from 1978 to 2005. In the presence of multiple simultaneous observations, one single instrument was selected. We go further by including all available datasets, and covering the period from November 8, 1978 to December 31, 2014. In addition, we provide a systematic framework for merging overlapping observations, filling in periods of missing data with solar proxies, and taking into account uncertainties, finally providing uncertainties for the composite too. The first stage, which consists in collecting all the datasets and preprocessing them to enable their merging has already been described by *Schöll et al.* [2016], henceforth referred to as Paper I.

In the current paper, we concentrate on the making of the SSI composite, including a time-dependent uncertainty of the datasets, and the properties of that composite. Two major assets of the mathematical procedure we propose are its traceability, and the decoupling of the statistical problem (merging SSI datasets) from the scientific one (correcting SSI datasets). Our method can be readily extended to other spectral bands, or to combinations of observations. **At this stage we merge the datasets without attempting to correct them. While the help of additional physical constraints and SSI models should lead to better results, we consider the making of a purely observational composite as an important and mandatory first step toward more elaborate composites.**

The paper is structured as follows. First, in Section 2, we briefly discuss the datasets used for the **observational** UV composite presented here. Then, in Section 3, we present in detail the tools to derive the composite. Third, in Section 4, **we present an experimental version of the SSI composite, labelled *SOLID.beta*, and compare it with available SSI reconstruction models. In Section 5, we discuss remaining issues, which are solved in Section 6, where we present the final version of the observational composite.** Then, in Section 7.1, **the response of atmospheric heating to the SOLID composite is evaluated and compared against other SSI products.** Finally, in Section 8, we summarize our findings and list the specific actions that remain to be taken before the composite can be truly considered as being representative of the solar UV variation.

2. SSI observations

Our composite is based on 20 instruments, which are listed in Table 2. In addition, we also took into consideration 9 reference spectra, of which - due to the unknown uncertainty of the other datasets - we only used one, i.e. the ATLAS3 spectrum, and 6 solar proxy datasets, as listed in Table 1. In Paper I, we describe how they are all converted into a unified format, together with independent uncertainty estimates. Several instruments were not included in our composite. ENVISAT/SCIAMACHY, for example, was excluded **at this stage** because it is not degradation corrected. The broadband filter radiometers SOHO/VIRGO-SPM, PROBA2/LYRA, and PICARD/PREMOS also were also omitted because of their coarse spectral resolution. However, these instruments are valuable for validating the SSI composite, as discussed in Section 5.

Let us stress that none of the original SSI datasets and proxy datasets has been corrected or adjusted as our prime objective is to build a composite that is as objective as possible, before considering what changes will be needed to enhance its value for climate studies. For the same reason, we deliberately excluded inputs coming from model reconstructions of the SSI. While this questionable choice inevitably leads to discrepancies between some of the instruments, it is also an asset, in the sense that it provides us with a fully independent reference dataset for testing models and checking individual instruments. The time-dependent uncertainties are furthermore evaluated by independent means, thus ensuring that all the instruments can be meaningfully compared. This is important for what follows because these uncertainties determine the contribution of each instrument to the composite.

In addition to SSI observations, we consider 6 solar proxies. While they do not strictly correspond to SSI observations, they are known to reproduce SSI variations in given bands, and for specific time scales. The 10.7 cm radio flux (or F10.7 index), for example, has been widely used as a proxy for the EUV band, whereas the 30 cm flux is better suited for reproducing the solar rotational variability at longer UV wavelengths [*Dudok de Wit et al.*, 2014]. The sunspot darkening is a proxy that has been successfully used to reproduce the variability in TSI [*Fröhlich and Lean*, 2004].

This list does not include the MgII index, which is a widely-used proxy for solar variability in the UV [*Viereck et al.*, 2001]. Indeed, while we concentrate here on the space age only (from 7 November 1978 onward), the full SOLID dataset actually starts in 1950, thus requiring proxies that cover the full period. Most radio fluxes are available for that period, whereas measurements of the MgII index started only in November 1978. This is the reason why for this first version of the SOLID dataset, we did not include the MgII index. Incidentally, because the MgII index is highly correlated with radio fluxes at 15 and 30 cm, most of its variability can be adequately reproduced with a combination of radio fluxes at these two wavelengths [*Dudok de Wit et al.*, 2014].

Resorting to proxies is also questionable choice, but it is the only solution for filling in the numerous data gaps in the composite, while relying on observations that have been shown to be good substitutes for the SSI. Of course, one should interpret such proxy reconstructions with great care when considering time scales in excess of several years, for which they may not properly capture the true solar variability.

2.1. TSI dataset

TSI observations are formally part of the SSI. However, they have received considerably more attention so far, and expectations are high regarding a potential long-term variability, whose assessment requires extra care. For that reason, we processed the TSI independently, and **built its composite** without resorting to proxy data, or TSI models. We also used slightly different approach, which is detailed in a companion paper [*Dudok de Wit et al.*, 2017].

Table 1. Proxies used in addition to the original SSI data in order to fill in data gaps.

Name of proxy	Origin (Observatory)	relevant for
30.0 cm radio flux	Nobeyama/Toyokawa	UV
15.0 cm radio flux	Nobeyama/Toyokawa	UV
10.7 cm radio flux	Penticton/Ottawa	EUV/UV
8.2 cm radio flux	Nobeyama/Toyokawa	EUV/UV
3.2 cm radio flux	Nobeyama/Toyokawa	EUV/UV
sunspot darkening	Greenwich/SOON netw.	VIS

Table 2. List of the instruments used for making the composite, the version of the dataset, if available, as used in the SOLID composite; see Paper I for more details. The observation period corresponds to the data as they are used in the SOLID composite.

Instrument	Version	Wavelength range [nm]	Observation period [mm/yyyy]	Reference
GOES13/EUVS	n.a.	11.7–123.2	07/2006–10/2014	*Evans et al.* [2010]
GOES14/EUVS	n.a.	11.7–123.2	07/2009–11/2012	*Eparvier et al.* [2009]
GOES15/EUVS	n.a.	11.7–123.2	04/2010–10/2014	*Eparvier et al.* [2009]
ISS/SolACES	n.a.	16.5–57.5	01/2011–03/2014	*Schmidtke et al.* [2014]
NIMBUS7/SBUV	n.a.	170.0–399.0	11/1978–10/1986	*DeLand and Cebula* [2001]
NOAA9/SBUV2	n.a.	170.0–399.0	03/1985–05/1997	*DeLand et al.* [2004]
NOAA11/SBUV2	n.a.	170.0–399.0	12/1988–10/1994	*Cebula et al.* [1998]
SDO/EVE	5	5.8–106.2	04/2010–10/2014	*Woods et al.* [2012]
SME/UV	n.a.	115.5–302.5	10/1981–04/1989	*Rottman et al.* [1982]
SNOE/SXP	n.a.	4.5	03/1998–09/2000	*Bailey et al.* [2000]
SOHO/CDS	3.1	31.4–62.0	04/1998–06/2010	*Harrison et al.* [1995]
SOHO/SEM	n.a.	25.0–30.0	01/1996–06/2014	*Wieman et al.* [2014]
SORCE/SIM	21	240.0–2412.3	04/2003–05/2015	*Rottman et al.* [2005]
SORCE/SOLSTICE	13	115.0–309.0	04/2003–05/2015	*Rottman* [2005]
SORCE/XPS	10	0.5–39.5	04/2003–05/2015	*Woods and Rottman* [2005]
TIMED/SEE-EGS	11	27.1–189.8	02/2002–02/2013	*Woods et al.* [1994]
TIMED/SEE-XPS	11	1.0–9.0	01/2002–11/2014	*Woods et al.* [1999]
UARS/SOLSTICE	11	119.5–419.5	10/1991–09/2001	*Rottman et al.* [1993]
UARS/SUSIM	22	115.5–410.5	10/1991–08/2005	*Brueckner et al.* [1993]

3. Methodology

The approach we advocate for this is a probabilistic one, in which, at each time step, we consider a weighted average of the different observations. These weights are set by the uncertainty of the observations, for which we thus need a metric that can be consistently applied to all the observations.

An important and novel feature of our approach is its multi-scale character. Simultaneous observations may agree on one particular time scale, and diverge on another one. Among the most debated examples is the difference between the SORCE/SOLSTICE and SORCE/SIM instruments at 240 nm [*Lean and DeLand*, 2012]: both show the same solar rotational variability, but disagree on the presence of a long-term trend. In such a case, direct averaging of the two will mix instrumental artifacts with the solar signal, rather than keep the best of each record. Likewise, it is important to take into account the disparity in the quality of the different datasets by assigning to each of them a time-dependent (and also time scale-dependent) uncertainty. **Another motivation for working scale-by-scale is the occurrence of artificial jumps in the composite whenever different datasets with data gaps are directly averaged.**

As we shall show below, the uncertainty of the datasets is a crucial ingredient of our composite because it allows to weight co-temporal observations at the same wavelength. Ideally, such uncertainties should be provided by the instrument teams. In practice, they are often absent or lack a crisp definition, and therefore cannot be meaningfully compared. Since we need to rely on the same definition for all datasets, we decided to use instead an independent estimation of the uncertainty (see Sec. 3.1) and use it to assign weights.

Our uncertainty is inherently scale-dependent; its high-frequency part (called precision) is the easiest to estimate. We also require a long-term uncertainty and call it stability (Sec. 3.2). The multi-scale approach allows mixing precision and stability at each scale in a natural way. The heuristic idea is as follows: at a specific timescale, every sample incorporates information over a time-interval that is proportional to its scale. As such, the uncertainty at this scale includes both the precision over this time-interval, as well as the stability over the same time-interval weighted by the timescale. As a consequence, the contribution of the precision to the uncertainty decreases with larger time-scales, while the contribution of the stability increases in proportion to the scale.

The creation of the composite involves a multiscale decomposition of the records, followed by a weighted average, and finally the recombination of the different scales. In practice, this procedure requires five steps, which we detail below.

The first direct spectral observations available are from the NIMBUS7/SBUV instrument, which started to provide data in November 8, 1978. Therefore, all datasets are extended back in time to that date and cover the time up to December 31, 2014.

3.1. Precision

In this work we use the term *precision* to quantify in each SSI dataset the high-frequency noise component that is routinely associated with random instrumental fluctuations. **The associated timescales are 3-4 days and below.** As described in Paper I, we determine the precision by using an adapted version of the wavelet noise estimator by *Donoho and Johnstone* [1995]. Let us note, however, that this estimator cannot properly quantify low frequency noise **(i.e. on time scales of several days and beyond)**, and therefore is not suited for observations that are contaminated, for example, by red noise. For that purpose, we consider a second, and different estimator, i.e. the long-term uncertainty estimate as discussed in the following.

3.2. Long-term uncertainty

Beyond the uncertainty caused by the short-term noise, referred to as precision here, an additional uncertainty of the measured irradiance comes from the evolution of the instrument's response in time. The instrument's response can change because of the instrument's (detector or filter) degradation, also called *ageing*, but also when changes in the operations of the spacecraft or instrument affect the measurement. When these effects are identified and/or understood, they can be corrected. However, it is not rare that SSI datasets have residual instrumental effects that remain in the signal as part of the real SSI time evolution. The uncertainty on the SSI dataset caused by these effects can be referred to as *long-term precision* or *stability*. We use here the term of stability.

It is out of reach to identify and correct *a posteriori* the instrumental effects affecting the time evolution of the observed SSI. Here, we estimate the uncertainty on SSI time series (i.e. the stability) by **comparing the latter to a two**

time-scale proxy model, and identifying patterns that cannot be reproduced by that very admissible model. More precisely, for each instrumental record $I(\lambda, t)$ we determine the high-frequency and low-frequency coefficients, a_i^{LF} and a_i^{HF}, respectively, of the following model

$$I(\lambda, t) = a_0 + \sum_{i=1}^{n} (a_i^{\mathrm{LF}} P_i^{\mathrm{LF}}(t) + a_i^{\mathrm{HF}} P_i^{\mathrm{HF}}(t)) \qquad (1)$$

where the summation is over different solar proxies P_i and the superscript LF and HF represents the low and high frequency component, respectively. These components are determined using a running average of 108 days, *i.e.*, four solar rotations, a duration that is similar to the lifetime of active regions on the Sun. Using the more traditional 81 days to distinguish short and long timescale does not affect the results, and we found that, qualitatively, 108 days allows to better isolate the long term variations that can include instrumental trends.

It is known that using a 2-time-scale reconstruction model generally improves the fitting of observed time series [*Woods et al.*, 2000]. To build this admissible proxy model we use 6 proxies: the Daily Sunspot Area [*Wilson and Hathaway*, 2006, DSA], the Mg II index [*Skupin et al.*, 2005] and the radio fluxes at 3.2 cm, 10.7 cm, 15 cm, and 30 cm [*Dudok de Wit et al.*, 2014]. Clearly, the larger the number of simultaneous proxies, the larger the number of degrees of freedom in the model, and the more the model might reproduce non-solar variations. One can therefore decide to be more or less allowable in asking the true SSI to be reproducible by proxies.

Once the observed time series is fitted with this proxy model over the whole record, **we estimate its stability empirically by**

$$s(\lambda, t, \tau) = |\mathrm{slope}(I_{\mathrm{obs}}, t) - \mathrm{slope}(I_{\mathrm{fit}}, t)|, \qquad (2)$$

where the slope is computed over a chosen time interval τ. The stability is therefore time-dependent and it is given in $\mathrm{Wm}^{-2}\mathrm{yr}^{-1}$ (or, **alternatively**, in $\%\mathrm{yr}^{-1}$). This stability represents the ability of a proxy model, adjusted at each time series, to reproduce the observed slope computed over a dedicated time interval τ, which thus also sets the time scale at which the stability is considered. Here we estimate it for a time scale of $\tau = 3$ years in order to focus on trends.

3.3. Temporal extension of SSI datasets

The multi-scale decomposition can only be performed on regularly sampled time series with no missing data. Following the pre-processing stage that is described in Paper I, our input data are SSI time series with daily values, with one record for each 1 nm wavelength bin.

Prior to decomposing the data, we extend each dataset over the interval going from November 8, 1978 to December 31, 2014 in order to make all records of equal length. **This preparatory step has not been covered Paper I**. We fill in the data gaps by expectation-maximization [*Dudok de Wit*, 2011]. This technique exploits the correlation between specific bands of the SSI and the above-mentioned solar proxies to replace missing values by a linear combination of the latter, after prior decomposition into two different time scales with a cutoff at 81 days. Two separate time scales are needed to properly handle the possibility for the same solar features, such as sunspots, to cause darkening (in the visible), and brightening (in the UV). The 81-day cutoff is commonly used to separate fast variations from slow ones [*Woods et al.*, 2000].

After extending the SSI datasets, we end up with one large table that has 13202 time steps, and as many columns as there are individual wavelengths multiplied by the number of instruments, i.e. typically 10^7 records. Let us stress that this temporal extension is required only to decompose the data into different time scales and as such is a technical necessity; the interpolated or extrapolated values enter the composite with a lowered weight, as they are assigned a higher uncertainty.

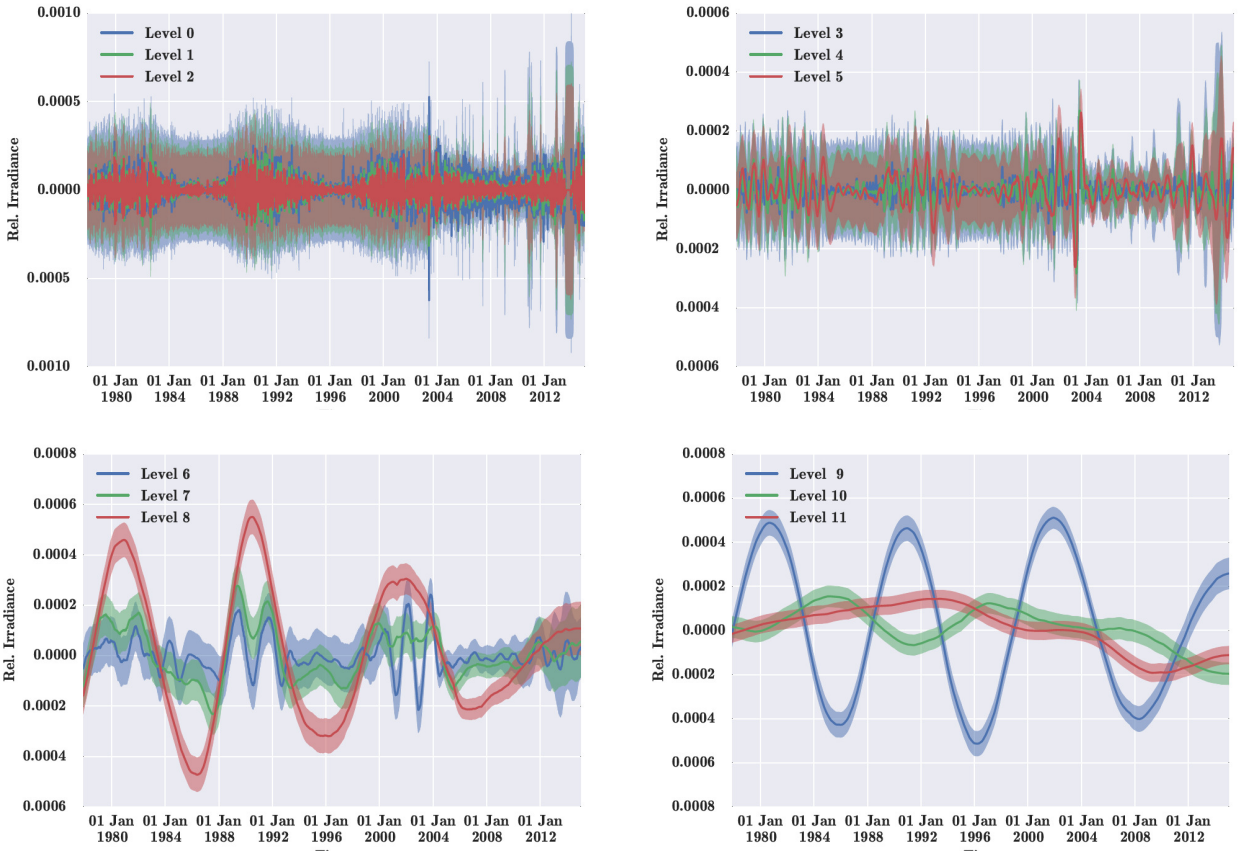

Figure 1. Illustration of the multiscale decomposition of the **extended** SORCE/SOLSTICE data set at 220.5 nm for Levels 0, 1, and 2 (top left), Levels 3, 4, and 5 (top right), Levels 6, 7, and 8 (bottom left), and Levels 9, 10, and 11 (bottom right). Level 12 with a scale of $a^{12} = 4096$ days is not shown as it represents a quasi-constant offset.

3.4. Multiscale decomposition of the SSI records

The natural tool for decomposing time series into different time scales is the wavelet transform, which decomposes each time series into $J+1$ different records of identical length. Their characteristic scales $a = 2^j$ are numbered by their level $j = 0, 1, 2, \ldots, J$. The largest level J is the largest integer such that $a_J = 2^J \leq d$, where d is the duration (in days) of the record.

This wavelet decomposition can be performed in different ways. We need an undecimated (or redundant) transform, so that a precise time stamp can be assigned to each wavelet coefficient. The transform should also be orthogonal in scale, so that operations performed on the wavelet transform at one particular scale do not affect neighbouring scales. The solution we advocate here, which is widely used in astrophysics, is based on the one-dimensional *à trous* wavelet transform [*Starck et al.*, 2010].

We decompose the time series $d_\lambda(t)$ at wavelength λ and time t into multiple orthogonal time series $d^*_{j,\lambda}$ by convolving it with a Gaussian kernel $\mathcal{G}(t)$ of width (scale) $a = 2^j$, as given in Eq. 3:

$$d^*_{j,\lambda}(t) = d_\lambda(t) \star \mathcal{G}(t, 2^j) \; . \tag{3}$$

For the lowest level $a = 1$ we just take $\mathcal{G}(t, a = 1)$ as the identity function on t, so that

$$d^*_{0,\lambda}(t) = d_\lambda(t) \tag{4}$$

Boundaries are handled by mirroring the data on each side. The wavelet transform at level j now reads

$$d_{j,\lambda} = \begin{cases} d^*_{j,\lambda} - d^*_{j+1,\lambda} & \text{if } \; j < J \\ d^*_{j,\lambda} & \text{if } \; j = J. \end{cases} \tag{5}$$

One advantage of this method is the easy recovery of the original time series d_λ simply by adding up its wavelet transforms $d_{j,\lambda}$. Indeed,

$$d_\lambda = \sum_{j=0}^{J} d_{j,\lambda} \ . \tag{6}$$

At each level j, both precision and stability contribute to the combined uncertainty. While the precision decreases with larger scales due to the noise averaging out over a larger time-period, the uncertainty associated with the stability increases towards larger scales. What would be really needed here is an estimate of the uncertainty versus time-scale. For the TSI *Dudok de Wit et al.* [2017] find the power spectral density of the uncertainty to be **proportional to** the inverse of the frequency (with frequency $= 1/a$), as with so-called 1/f noise, or shot noise. This scaling may not apply to the SSI, whose instruments have different noise characteristics. For that reason, we rely **here on the precision and an empirical stability estimate to obtain the uncertainty** at all scales.

We estimate the uncertainty $\epsilon_{\lambda,j}(t)$ at level j by using a weighted spectrum of the squared precision $\epsilon^2_\lambda(t)$, together with a weighted and scaled sum of the stability $s_\lambda(t)$, where the weights are the Gaussian kernel for both precision and stability and the stability is scaled proportional to the kernel width a.

$$\epsilon_{j,\lambda}(t) = \sqrt{\left(\epsilon_\lambda(t) \star \mathcal{G}(t, 2^j)\right)^2 + \left(a\ s_\lambda(t) \star \mathcal{G}\left(t, 2^j\right)\right)^2} \tag{7}$$

As an example of the decomposition of the SSI data records Figure 1 shows the SSI time series and their respective uncertainties for Levels 0, 1, 2 (top left), Levels 3, 4, 5 (top right), Levels 6, 7, 8 (bottom left), and Levels 9, 10, 11 of the **extended** SORCE/SOLSTICE time series **(the result after applying the steps as described in Sec. 3.3)**, at 220 nm.

In the following we keep the uncertainties **for each time scale** constant in time, although the method can easily handle time-varying uncertainties. **In particular, we can incorporate information from the instrument teams and, for example, increase the uncertainty during times when the spacecraft has off-pointing problems. Such adjustments can also be made at specific time-scales if the observations are known to be affected by band-limited noise. In future version of the dataset, this will be considered, for example for observations by ENVISAT/SCIAMACHY. This instrument adequately reproduces solar variability at short time scales (days to months) but its long-term variability suffers from several interruptions that occurred during its lifetime. When several cotemporal observations with differing variations are averaged, it is eventually their uncertainty which determines how each of them will be weighted. Therefore, it is of great importance to properly estimate such uncertainties by injecting physical information in them. In doing so, we decouple the scientific problem (*What prior information goes into the composite?*) from the statistical one (*What is the best way of making the composite?*). Clearly, the first problem is open-ended, and here we focus on the second one.**

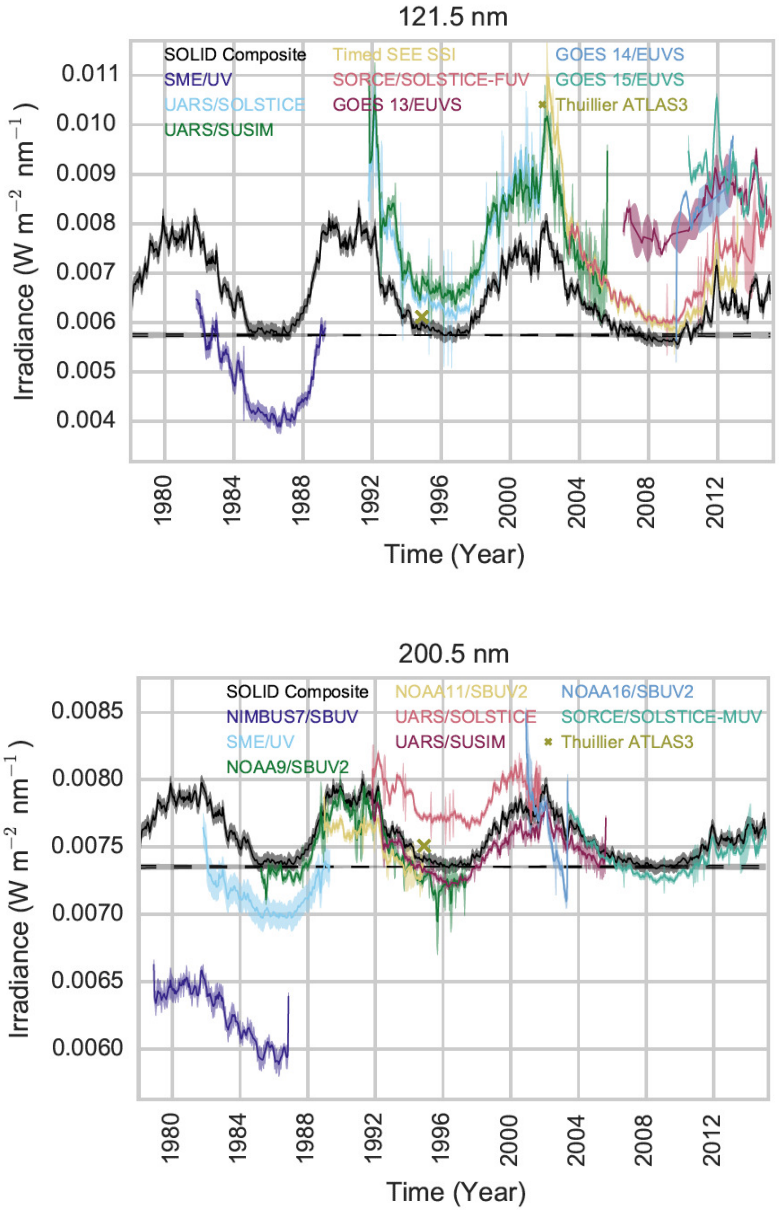

Figure 2. SOLID composite along with the individual irradiance datasets that are used to produce it, shown at 121.5 nm (top panel) and 200.5 nm (bottom panel).

3.5. Averaging the wavelet transformed data

Once we have performed the multiscale decomposition, $d_{j,\lambda}$, of the SSI for each level j (and instrument I, not indicated here), we determine the composite by maximizing its likelihood, which is equivalent to making a weighted average of the values of $d_{j,\lambda}$; the weights are given by the inverse variance of each record. **This is done scale-wise.** The uncertainty of the composite can be obtained by classical error propagation. Thanks to the orthogonality of the wavelet transform, uncertainties at different scales can be processed separately, and added as if they were independent.

The equations to derive the scale-wise components, $\bar{d}_j$, of the composite for each level j and its respective uncertainties, $\bar{\epsilon}_j$, again for each level j are

$$\bar{d}_j = \sum_{i \in \mathrm{I}} d_{i,j} w_{i,j} \tag{8}$$

$$\bar{\epsilon}_j = \left(\sum_{i \in \mathrm{I}} \epsilon_{i,j}^2 w_{i,j}^2 \right)^{1/2} \tag{9}$$

$$\text{where } w_{i,j} = \frac{\epsilon_{i,j}^{-2}}{\sum_{k \in \mathrm{I}} \epsilon_{k,j}^{-2}} \ .$$

are the weights for level j and instrument i for the wavelength of interest, and $\epsilon_{i,j}$ is the corresponding **uncertainty** at level j. As described in Paper I, we assume purely uncorrelated noise. Therefore, for interpolated and proxy-extended data, after flagging them, we increase the **uncertainty** to the 1-σ standard variation of the actual variation of the SSI data of that dataset **scaled with the $\sqrt{N}$, with N being the number of missing days determined from the onset and end of the data gap.** This results in a substantially lower weight of the interpolated and extrapolated data values in the composite.

3.6. Combining the reconstructed scales

To obtain the final composite, the components of the composite are summed-up scale-wise (i.e. over all levels), as given in Eq. 6. The uncertainty, ϵ_{comp}, of the final composite is obtained by error propagation

$$\epsilon_{\mathrm{comp}} = \left(\sum_{j=0}^{J} \bar{\epsilon}_j^{\,2} \right)^{1/2} \ . \tag{10}$$

3.7. Absolute scale of composite

The above procedure results in a time series that combines all available instruments while taking into account the uncertainty of the individual datasets, with both precision and stability. However, the absolute scale also needs to be set. To do so, we re-calibrate the composite to the ATLAS 3 reference spectrum by *Thuillier et al.* [2004] and, at the same time, constrain it to the TSI composite by *Dudok de Wit et al.* [2017] for that particular day when the reference spectrum was measured.

First, we re-scale the ATLAS 3 reference spectrum to make its integrated spectrum match the value of the TSI composite for the day of the ATLAS 3 observation. For this, we first use a black-body model to the unobserved infrared tail of the spectrum, and succesively scale the integrated spectrum to the TSI composite. Secondly, we use this modified ATLAS 3 spectrum to re-scale the value of the SOLID composite such that it matches the reference spectrum for its date of the observation.

4. Preliminary observational composite

In the following, we present the **first, preliminary**, observational SSI composite for different wavelengths **and daily resolution** along with the UV datasets that went into the production of the composite. **For practical reasons we set the spectral resolution to 1 nm, but at the longer wavelength ranges (starting at 623 nm) we have a coarser resolution of 2 nm and higher.** Figure 2 shows the observational composite and the available observations it is made of for 121.5 nm (top panel) and 200.5 nm (bottom panel). As expected, the composite closely corresponds to a weighted average of the individual records. Note that most records agree well on their short-term variability, and less so on the long term, hence the importance of merging them scale-wise. Thanks to this multi-scale approach, and to the use of solar proxies for filling in gaps, the stability of the composite is better than what would have been obtained by simply daisy-chaining the records. Most observations and the composite agree better at short wavelengths, where the larger relative variability results in a more favorable signal-to-noise ratio. There are some exceptions, however. At 121.5 nm, for example, the solar cycle variability of SME exceeds that of the other instruments, which suggests the needs for a correction, as already reported by *Woods et al.* [2000]. **One side effect of the use of proxies is their small but significant contribution to the composite. This is evident, for example, in the variation of the Lyman-α line: the large excursion observed in mid-1992 is smaller in the composite than it is in the original observations from UARS/SUSIM. One could easily reduce this contribution from proxies and even set it to 0 if there are cotemporal observations available, as we did for making the TSI composite [*Dudok de Wit et al.*, 2017]. However, for spectral bands that suffer from fragmented observations or from a low signal-to-noise ratio (especially above 300 nm), proxies help constrain the composite.**

Figure 3 compares the observational composite with various existing reconstructions and the SORCE Solar Sprectral Irradiance dataset[1] for the following spectral bins: 120–122 nm, 130–200 nm, 200–242 nm, 242–310 nm, 300–350 nm, 350–400 nm, **400–500 nm, and 500–600 nm**. The reconstructions we consider are from the semi-empirical SATIRE-S model [*Yeo et al.*, 2014], the empirical NRLSSI1 model [*Lean*, 2000] and its more recent version NRLSSI2 [*Coddington et al.*, 2016], **and direct observations from SORCE/SOLSTICE and SORCE/SIM as part of the SORCE Solar Irradiance dataset. In this dataset, SIM observations are used from 310 nm onward.**

The first message coming from this figure is the good agreement between the composite and the three mod-

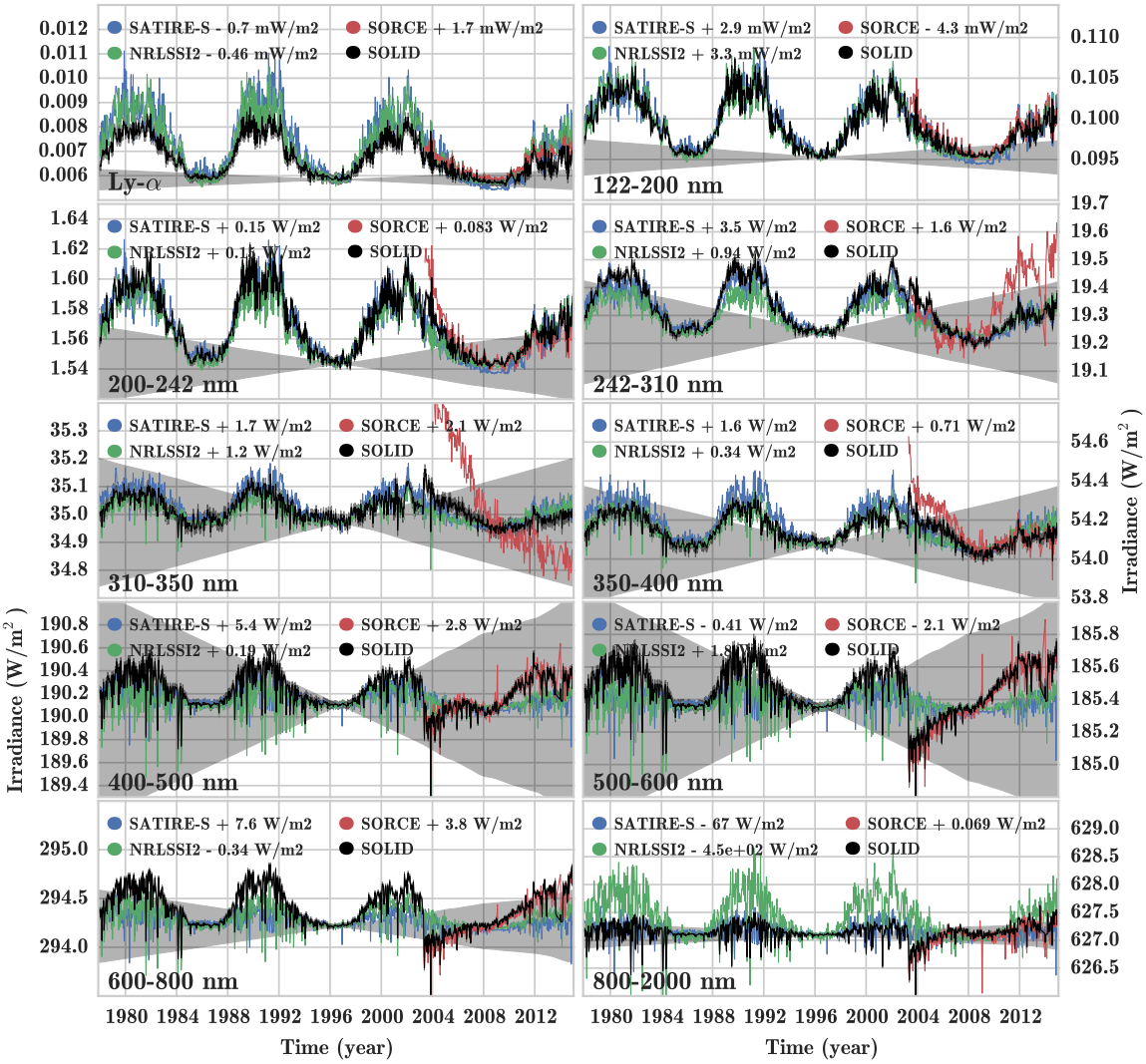

Figure 3. Illustration of the observational SOLID composite (black line), model reconstructions from NRLSSI1 (green line) and SATIRE-S (blue line), and since 2003, the observations from the SORCE mission (red line), **with SIM being used from 310 nm onward**. These data are integrated over the following spectral intervals: Top row: 120–122 nm (left) and 122–200 nm (right); second row: 200–242 nm (left) and 242–310 nm (right); third row: 310–350 nm (left) and 350–400 nm (right); fourth row: 400–500 nm (left) and 500–600 nm (right); bottom row: 600–800 nm (left) and 800–2000 nm (right). The numbers in the legend given after the name of each dataset indicate the value for the absolute scaling of each of the datasets to the SOLID composite. The gray-shaded area illustrates the cumulated uncertainty of the SOLID composite starting from January 1, 1996.

els **for the spectral ranges from 120 − 310 nm (the top 4 panels), for none of which it** significantly deviates from, given its confidence intervals. This highlights the difficulty in assessing differences between these models when they are as poorly constrained by the observations. **This also highlights** the need for a sound assessment of the confidence intervals. Clearly, future improvements of the composite should not depend on the individual datasets alone, but also on refinements that will be made in the precision and stability estimates.

The second message is the unusual solar cycle variability of the composite after 2003, when SORCE/SIM data start being used. As long as there are alternatives to these observations (i.e. for 200–**400** nm, and at lower wavelengths), the composite remains in good agreement with the models. At **longer** wavelengths, when SORCE/SIM is the only observing instrument,

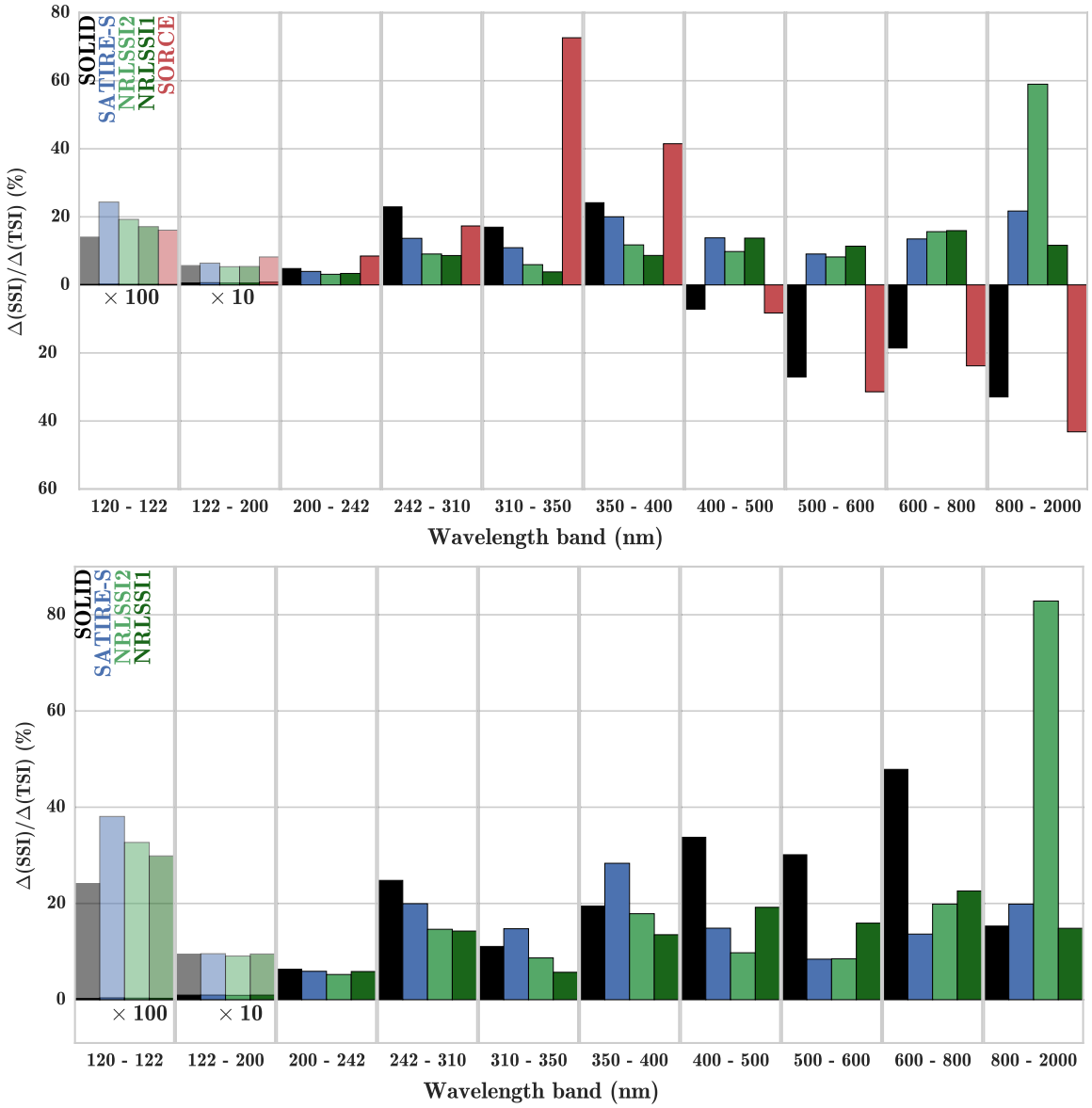

Figure 4. Upper Panel: Change of the annual mean of SSI in different spectral bins from 2003 to 2008 with respect to the variation in TSI for the same time interval. Shown are the relative changes for SOLID.beta (black), SATIRE-S (blue), NRLSSI1 and NRLSSI2 (dark and light green), and the SORCE composite (red) **with SIM being used from 310 nm onward**. For better illustration, the first and second spectral bin, i.e. for 121–122 nm and 130–200 nm is multiplied by a factor of 100 and 10, respectively, additionally shown in partly transparent color. Lower panel: Same as upper panel, but for the annual means of 1989 and **1996**, for which no SORCE data is available.

the discrepancy with the models, and with former solar cycles becomes striking, **which is in line with previous studies by *Cahalan et al.* [2010] and *Ermolli et al.* [2013]. As the observations from SIM data are the only to cover wavelengths longward of 410 nm we consider that particular dataset further in Sections 5 and 6.**

Figure 3 also illustrates the precision and stability of the composite as derived in Paper I and Sec. 3.2 by showing how it increases in time when moving away from a date that has been arbitrarily chosen to be in the center of the interval. The figure thereby reveals how weak the solar cycle variability becomes, as compared to the uncertainty, when moving from the UV to the visible. Note that this representation may actually overestimate the true long-term stability, which does not increase that fast in time. Indeed, for the TSI, *Dudok de Wit et al.* [2017] find that the stability does not increase linearly with time and so these commonly-used fan-shaped structures may need to be revised in future work.

A different representation of the composite is given in Figure 4, which shows the annual mean of the SSI vari-

ation relative to the TSI variation for the spectral intervals 120–122 nm, **122–200 nm, 200–242 nm, 242–310 nm,** 310–400 nm, 400–500 nm, 500–600 nm, 600–800 nm, and 800–2000 nm. **We note that the variability of the high-resolution spectrum shows much more detail, [see *Fontenla et al.*, 2015, Fig. 14] and [see *Ermolli et al.*, 2013, Fig. 6].** To better illustrate the variation of the SSI, Figure 4 shows the change in SSI relative to the change in TSI for the declining phase of solar cycle 23 (annual means from 2003 to 2008 – upper panel) and solar cycle 22 (annual means from 1989 to **1996** – lower panel). For better visibility, the 120–122 nm and 150–200 nm spectral bins are scaled with a factor of 100 and 10, respectively.

For both time intervals, the variation in the Lyman-α line (i.e. the 120–122 nm band) is lowest for the SOLID composite, and highest for SATIRE-S, with NRLSSI2 and NRLSSI1 being in between. **The reason for this is the absence of rescaling of the SME data, whose values are approximately 1.5 times smaller than its expected level [*Woods et al.*, 2000]**. The absence of correction explains the lower solar cycle variability of the SOLID composite as compared to the Lyman-α composite by *Woods et al.* [2000]. We stress again that we took the approach to not change the original observations, with all the consequences this might have.

For the 130–200 nm and 200–242 nm wavelength ranges the variation of all datasets is very close, with a slightly higher variation for the SORCE dataset. Moreover, for the wavelength range 242–310 nm and both time intervals the SOLID composite gives the highest variation, while SATIRE-S, NRLSSI2 and NRLSSI1 give a lower variation.

Then, for the 310–350 nm and 350–400 nm wavelength ranges and for the 2003–2008 time interval the SOLID composite again gives the highest variation, and the variation is successively lower for SATIRE-S, NRLSSI2 and NRLSSI1. In this case, for both spectral ranges, the SORCE variation gives a considerably larger variation than all other datasets. For the 1989–**1994** time interval the variation of the SOLID composite is between the SATIRE-S and NRLSSI2.

And finally, for the 2003–2008 time interval, and the 400–500 and 500–600 nm range, the SOLID and SORCE composite give a negative solar cycle variation, while SATIRE-S, NRLSSI2 and NRLSSI1 show a variation in phase with the solar cycle. The reason is that for this time frame and wavelength range the only dataset available is SORCE/SIM. Therefore, the SOLID composite follows the overall variation as observed by the SORCE/SIM instrument. Whether the unusual variation reported by SIM is real or not is still an open question.

5. Validation of SSI composite

Let us now concentrate on recent observations when SORCE was operating. For that period, the SOLID composite compares well with the observations made by the PREcision Monitoring Sensor [*Schmutz et al.*, 2009] onboard the PICARD mission [*Thuillier et al.*, 2006]. Figure 5 shows the SOLID composite convolved with the broadband filters of the PREMOS instrument and the PREMOS observations [*Cessateur et al.*, 2016] centered at 210 nm (left panel) and 215 nm (right panel). The agreement between both time series for the two wavelength channels is excellent. In particular the temporal evolution of the rotational variability is in very good agreement. Some deviation after however can be seen in the 210-nm channel after 05/2012, and in the 215-nm channel from early 2013 onward. At 210 nm *Cessateur et al.* [2016] find a similar deviation when comparing the PREMOS data with SORCE/SOLSTICE (see their Fig. 13). **We emphasize here that for the comparison shown in Fig. 5 both datasets are in absolute values, and both the PREMOS channels and the SOLID composite are not detrended, i.e. they include the long-term trend. Due to the limited spectral coverage of the PREMOS data this can only be considered as a limited validation.**

Clearly, an issue **with the composite is the variability in the** 400–500 nm and 500–600 nm spectral bins. The only observations available for these spectral bins are from the SIM instrument, and these data have already been discussed controversially, **see e.g. [*Haigh et al.*, 2010]. While *Merkel et al.* [2011] conclude from their analysis of observations from the Microwave Limb Sounder (MLS) and Sounding of the Atmosphere using Broadband Emission Radiometry (SABER) and Global climate modeling that a higher UV is consistent with the different ozone solar cycle trends across the stratopause, *Ball et al.* [2016] argue that a higher UV variability is incompatible with the Stratospheric Water and Ozone Satellite Homogenized (SWOOSH) and the Global OZone Chemistry And Related trace gas Data records for the Stratosphere (GOZCARDS) datasets.**

From Figs. 2 and 3 it becomes clear that the overall trend in the SIM data cannot be reproduced by the multi-scale analysis using the proxy data, as discussed above. On the one hand, it could be argued that the approach to extend the observational datasets, as described in Section 3, has limitations. In addition, the reason might be that the degradation correction of the SIM data is incomplete. As pointed out by *Ball et al.* [2016] the observed SSI trend **of the SIM instrument** is inconsistent with observed ozone trends. This highlights the need to add **additional** constraints to future versions of the SOLID composite.

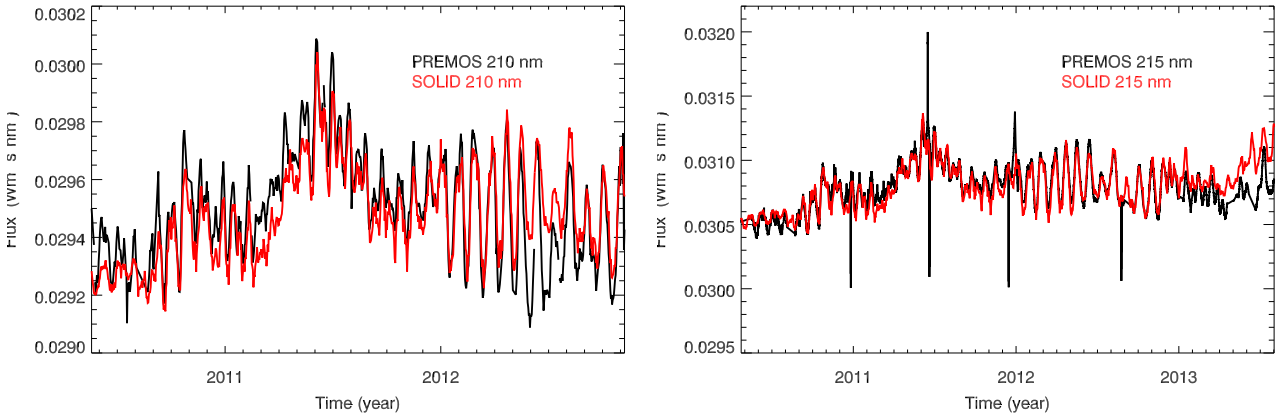

Figure 5. Comparison of the SOLID composite (red line) with the PREMOS observations (black line) for the 210-nm channel (left panel) and 215-nm channel (right panel).

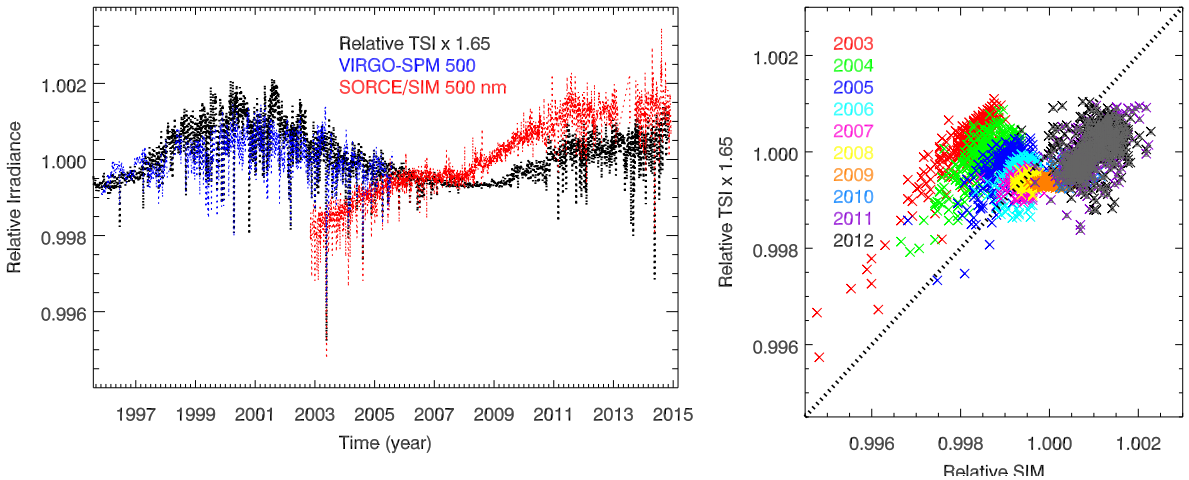

Figure 6. Left panel: comparison of the scaled TSI (black), the VIRGO-SPM 500-nm channel (blue), and SORCE/SIM at 500 nm (red). Following [*Wehrli et al.*, 2013] the relative TSI variability has been multiplied by the regression coefficient 1.65. **Right panel: scatter plot of the relative scaled TSI variation (black line in left panel) and the scaled SIM observations (red curve in left panel). The color code indicates the different years when the observations were taken. The dotted line is the line with slope equals 1, i.e. the expected gradient following *Wehrli et al.* [2013]. The datapoints for the years 2010 to 2012 (blue to black) that are employed in the revised SSI composite are additionally overlayed with grey triangles.**

In order to investigate this **further** we use an additional independent dataset that is not employed in the composite itself. First, we use data taken with the VIRGO-SPM instrument [*Fröhlich et al.*, 1995] onboard SOHO. *Wehrli et al.* [2013] investigated the correlation of the relative annual variability of VIRGO-SPM channels and TSI over the time frame of 2002 to 2012. Interestingly, the relative variation as observed with the VIRGO-SPM channel at 500 nm gave a statistically significant positive correlation with the relative variation of TSI, with a regression factor of 1.65 and a correlation coefficient of r^2=0.72.

Figure 6 shows the relative variation of the TSI scaled **with the factor** 1.65 (black) along with the relative variation **at** 500-nm channel of VIRGO-SPM, and the relative variation at 500 nm as observed with SIM (red). The discrepancy between the observations from SIM and the scaled TSI variation suggests that – at least for the early phase of the SORCE mission until approximately **2010 – a strong part of the variation seen by SIM may be instrumental. To further illustrate this, Fig. 6 (right panel) shows the corresponding scatter plot of the relative scaled TSI (black line in left panel) and the relative SIM observation at 500 nm (red line in left panel) for the years from 2003 to 2012, for which SIM observations are available. The color code illustrates the different years of the time series. This plot indicates that the behavior of SIM changed around 2010. While its SSI observations continuously increase, the TSI first decreases from 2003 until**

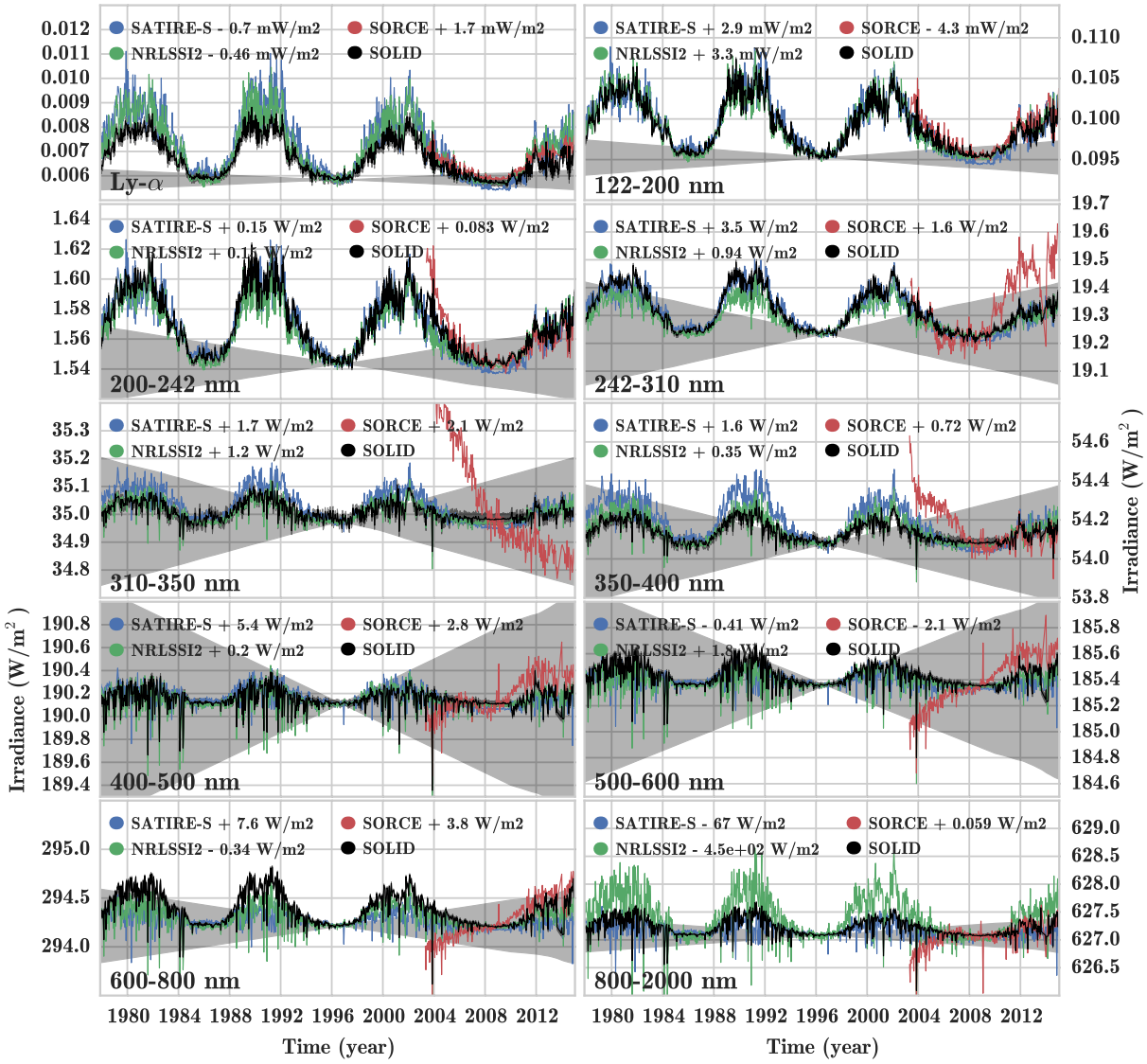

Figure 7. Same as Fig. 3 but for the final SOLID composite.

the solar minimum in 2008 and then increases with the onset of Solar Cycle 24. From *Wehrli et al.* [2013] we know that the SSI at 500 nm is - with high statistical significance - in phase with the TSI solar cycle variability. Therefore, we conclude that the SIM data before 2010 are likely to be unreliable and disregard them for our purposes. SIM seems to have recovered after 2010 and provides observations that are in phase with the TSI variability. So, for the remainder of this paper we shall only use SIM data from January 1, 2010 onward.

6. Final SSI composite

Based on the discussions in Sec. 5 we now provide the final version of the observational composite by only using SIM observations after 1 January 2010. All other observational datasets are kept as described above. Figures 7 and 8 show the relative contribution of the SSI in specific spectral ranges to the TSI. The figures are the same as Figs. 3 and 4 but for the final composite. Not surprisingly, the SOLID composite now also shows a variation from 400 nm onward that is in phase with the solar cycle. In the spectral range between 200–242 nm the SOLID composite is slightly higher than the models, but lower than the SORCE composite. For the spectral bins from 310–350 nm and 350-400 nm, the SOLID composite gives the lowest variation of all four (positively correlated datasets) datasets. For 400-500 nm the SOLID composite is slightly lower than the three models. The SORCE dataset shows a negative SSI contribution to TSI in this and all other spectral bins longward of that. For 500–600 nm the SOLID composite is almost identical to NRLSS1, while both SATIRE and NRLSSI2 give a slightly lower SSI variation. Then, for 600–800 nm the SOLID composite leads to the highest SSI contribution to the TSI variation. And finally, from 800–2000 nm SOLID is slightly higher than SATIRE while NRLSSI2 largely exceeds the other datasets, and NRLSSI1 gives the lowest SSI contribution.

Overall, the SOLID composite is an extremely valuable dataset to understand how to combine disparate observations, and test SSI models, as well as solar proxies. However, this dataset should be considered as the first step, **with multiple possible improvements.**

While the observational composite is consistent from a statistical point of view, future versions require additional physical knowledge to further reduce the impact of uncorrected instrumental artifacts. One obvious way of moving in that direction would be to build a hybrid dataset that combines observational and modelled SSI. Another important step is to correct some of the observational datasets for instrumental artifacts.

A thorough evaluation of the results and comparisons to observations will help not only to assess differences, weaknesses and strengths of the models, but also to advance knowledge and further understanding of the physical mechanisms that govern the influence of the Sun to the Earth's atmosphere and climate.

7. Sensitivity of atmospheric heating to the SSI dataset

7.1. Radiation scheme

To demonstrate the effects of the different spectra on the atmospheric energy balance, we performed calculations with the LibRadtran **v.2.0** high resolution model [***Emde et al.*, 2016**], which is a library of radiative transfer equation solvers widely used for UV and heating rate calculations (for a full list of relevant publications see http://www.libradtran.org). LibRadtran was configured with the pseudo-spherical approximation of DISORT solver, which accounts for the sphericity of the atmosphere, running in a six-streams mode. Calculations pertain to a cloud- and aerosol-free tropical atmosphere (0.56°N), the surface reflectivity is set to 0.1 and the effects of Rayleigh scattering are enabled. The atmosphere is portioned into 80 layers extending from the surface to 80 km. Here we show signals above 23 km. The model output is daily averages of spectral heating rates from 120 nm to 700 nm with a 1 nm spectral resolution for the 15$^{\text{th}}$ of January, calculated according to the recommendations for the Radiation Intercomparison of the Chemistry-Climate Model Validation Activity (CCMVal)[2]. Calculations were performed for NRLSSI2, SATIRE-S, **SORCE** and SOLID for solar maximum (2003) and solar minimum (2008) **years using the resolved solar spectra. That is in the 200-310 nm spectral band, which is important for ozone formation and absorption, NRLSSI2, SORCE and SOLID come in 1 nm bins whereas the resolution of SATIRE-S is 1 nm up to 289.5 and 2 nm thereafter. For this study the parts of the spectra that come with a coarser spectral resolution than 1 nm are interpolated linearly. As pointed out by *Deland and Cebula* [2012] a different resolution than the SORCE native resolution could introduce additional effects in the heating rate calculation for that dataset.**

The integrated difference between the solar maximum and solar minimum conditions is shown in Fig. 4a for specific spectral intervals. Since we are primarily concerned here with the direct effect of atmospheric heating, the ozone feedback is not considered and ozone mixing ratios are kept constant **to the climatology of a standard atmosphere** in all calculations. The ozone response to solar cycle variations in SSI and the impacts of the use of NRLSSI and SORCE spectral irradiance as forcing functions has been reported by ***Swartz et al.*** [**2012**], who provide a detailed evaluation of the individual mechanisms of atmospheric response to solar cycle variations in SSI through direct solar heating and photolysis.

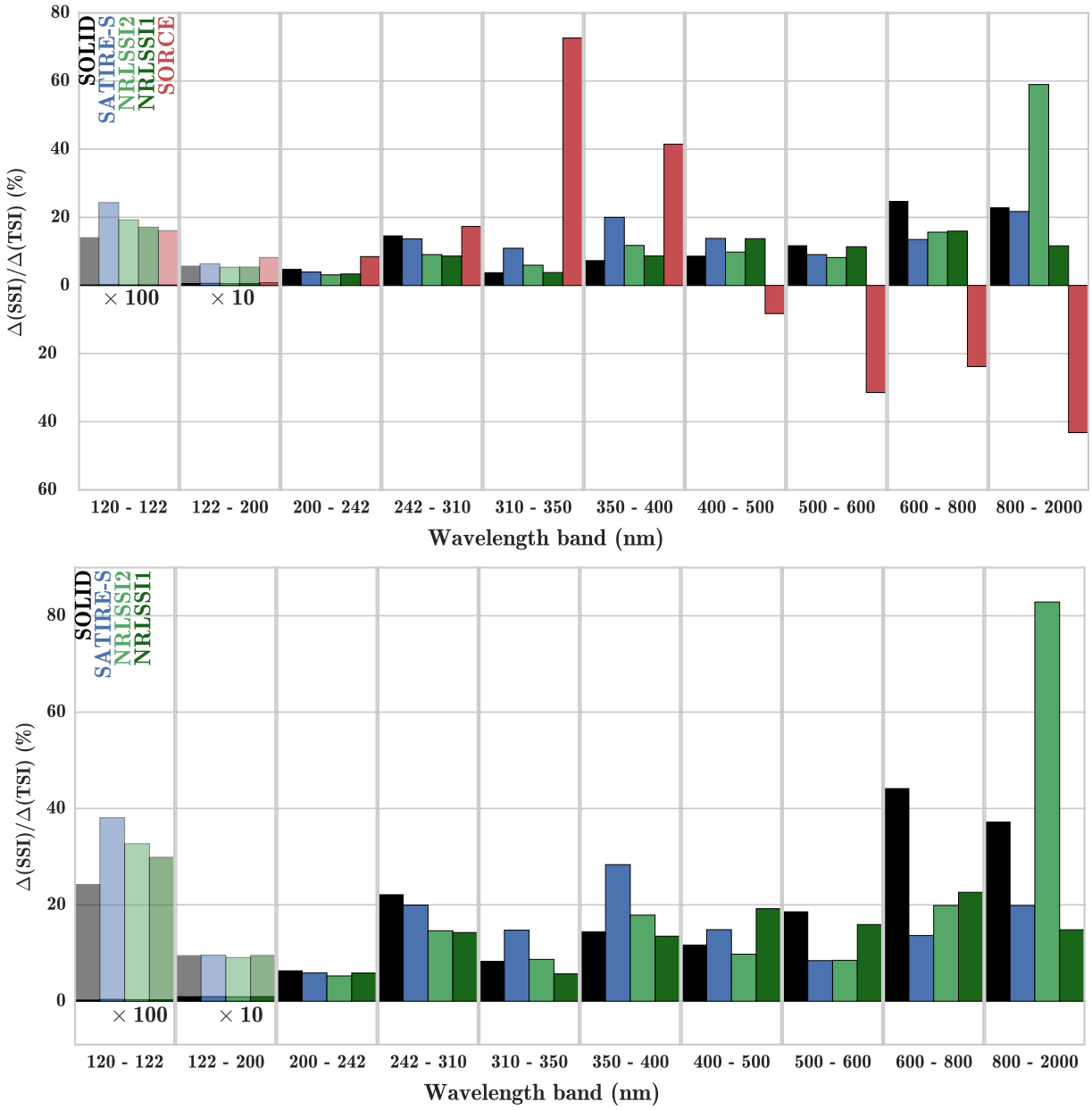

Figure 8. Same as Fig. 4 but for the final SOLID composite.

7.2. Effects in the Earth's atmosphere

Figure 9a compares solar cycle anomalies of total spectral heating rates (K/day), integrated from 120 to 700 nm, for all SSI datasets. The solar cycle signature in heating rates is characterized by two distinctive maxima in the stratopause (50 km) and upper mesosphere (above 70 km), resulting from the larger solar fluxes available for absorption by O_3 and O_2. The SOLID dataset introduces a solar-cycle related heating of about 0.12 K/day at the stratopause, which is considerably stronger than NRLSSI2 but weaker than SORCE. The difference in heating rates between SOLID and SATIRE-S is not statistically significant, if the uncertainty in the SOLID irradiances is taken into account (gray shading in Fig. 9a). The respective uncertainty of heating rate anomalies ranges from 0.09 to 0.14 K/day. **It should be noted that since UARS/SUSIM and UARS/SOLSTICE were taking measurements in 2003, their smaller amplitude for solar cycle variations below 310 nm moderates the SOLID forcing term relative to the SORCE-only forcing. This leads to weaker heating in the stratosphere between SOLID and SOLID.beta versions.**

The solar cycle heating in the mesosphere is related to absorption in the Lyman-α and the Schumann-Runge bands (175 to 200 nm) (Fig. 9b and Fig. 10). More specifically, irradiance changes in wavelengths between 130 and 200 nm contribute about 30-50% of the total solar heating above 70 km **in SOLID**, with weaker contribution at higher altitudes as the strong heating in

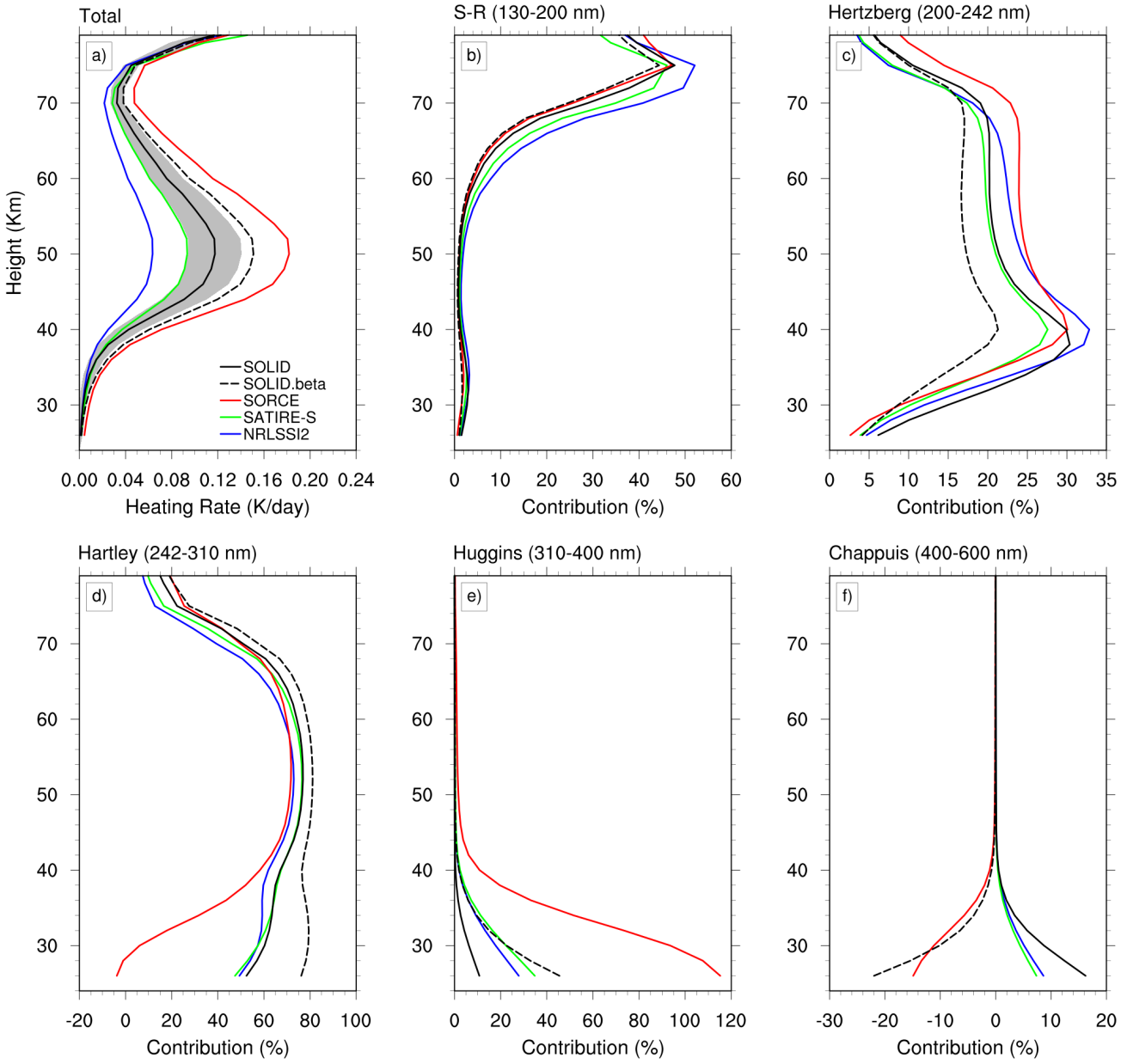

Figure 9. Comparison of solar heating rate differences (K/day) between solar minimum (2008) and maximum (2003) for the **SOLID (black solid), SOLID.beta (black dashed) composites,** NRLSSI2 (green), SATIRE-S (blue) and SORCE (red). Panel a) shows the integrated (120-700 nm) heating rate anomalies whereas panels b)-f) show the relative contribution (%) of the 130-200 nm, 200–242 nm, 242–310 nm, 310–400 nm and 400–600 nm intervals to the integral. Grey shading indicates the uncertainty in the total heating rate anomalies from the SOLID SSI uncertainty **(corresponding the to gray-shaded areas in Fig. 3)**.

Lyman-α **in not a part of the integral in Figure 9b.** NRLSSI2 shows a slightly stronger contribution in this region whereas SOLID.beta shows the weakest. Figure 9 indicates that anomalous heating in the stratosphere occurs primarily from 220 nm to 310 nm, as expected from the strong ozone absorption in the Hertzberg continuum (200 to 242 nm) and Hartley bands (242 to 310 nm). The heating rate anomalies in the stratosphere in the Hartley bands are **lower** in SOLID **compared to** NRLSSI2 and SATIRE-S, whereas SORCE shows the strongest anomalies at all heights and spectral bins except from about 290 to 310 nm (Fig. 10). **Nevertheless, SSI changes in this spectral region contributes almost the same to the total heating in all datasets (Fig. 9c,d).**

A notable difference of SOLID compared to the **other spectra** is the strong **positive** contribution between 400 – 600 nm (Chappuis bands, Fig. 9f) to the total heating of the lower tropical stratosphere. Solar fluxes in this spectral region **increase** by about 20-40 % from solar minimum to maximum. **On the other hand, SOLID.beta shows an opposite contribution with negative effect below 40 Km.** As described in **Sec. 4**, the reason is that the SOLID**.beta** variability in this spectral range is **essentially determined** by the SIM observations, which in a similar fashion show the same negative SSI change. **The assimilation of SIM observations after 2008 in SOLID now leads to a positive contribution, much stronger than NRLSSI2 and SATIRE, to balance the almost zero effect between 310-400 nm.** Although, the line-by-line calculations do not take into account solar fluxes in wavelengths above 700 nm, the out-of-phase variability in SOLID.beta and SORCE is expected to introduce negative heating rate anomalies in the lower stratosphere and troposphere, **as highlighted in other studies [*Cahalan et al.*, 2010]. Without taking into account the early part of SORCE/SIM observations, we find with SOLID a considerable positive influence in the heating of the lower stratosphere stemming from the Chappuis bands, where, nevertheless the total heating is negligible. Yet, this strong change in the visible may cause significant changes on the surface climate and should be examined with climate model simulations.**

The heating rate calculations of *Oberländer et al.* [2012] demonstrated a stronger solar cycle signal in the stratosphere for SATIRE-S compared to the first version of the NRL model. The SSI variability in NRLSSI2 still shows the weakest solar cycle signal as the heating rate anomalies at 50 km calculated with libRadtran are about 32% and 45% weaker than for SATIRE-S, SOLID respectively (Fig. 9a). As mentioned above, our interest lies in comparing the direct effects of SSI variability on atmospheric heating between the different SSI data sets, thus we have deliberately neglected the ozone feedback. This of course results to the underestimation of the total (radiative and chemistry) solar forcing effect on atmospheric heating, but allows for a more straightforward comparison, since the ozone response and the relevant combined effects strongly depend on **the relative contribution of wavelengths that photolyze molecular oxygen (<240 nm) and ozone (<310 nm), respectively** [e.g. *Haigh et al.*, 2010; *Swartz et al.*, 2012; *Ball et al.*, 2014]. *Gray et al.* [2009] estimated that the ozone feedback amplifies the direct radiative heating in the stratopause by more than 50% but it is less important in the middle stratosphere. On the other hand, the ozone effect was found dominant in the lower tropical stratosphere, contributing about 70–80% of the total solar cycle heating. **The calculations of *Swartz et al.* [2012] suggested for even a stronger contribution of ozone feedback on the total stratospheric heating, which adds up linearly to the direct heating throughout the middle and upper stratosphere. A comprehensive assessment of the combined radiative and chemistry contributions shall be made in a future study using a chemistry-climate model.**

8. Conclusion

In this study, we have introduced a novel framework for merging different SSI observations into one single homogeneous and continuous composite dataset. Here we combined observations from 20 instruments into a single composite with daily values from November 8, 1978 to December 31, 2014, running from 0.5 to 1991.5 nm, with most bins having a 1 nm spectral resolution. Three important assets of this composite are: 1) its reliance on uncertainty estimates of the instrumental data, which are derived in an independent way, and are used to weigh their individual contribution to the composite; 2) the estimation of the uncertainty of the composite itself, which is essential for testing it against model reconstructions; and 3) the objectivity and traceability of the method, in the sense that the contribution of each instrument, and at specific time-scales, can be controlled, and adapted if necessary.

The present composite is solely based on original (unadjusted) observations, as we consider this to be a mandatory first step toward more elaborate products that will require additional physical information in order enhance their scientific value. The list of obvious improvements includes:

- improve the uncertainty estimates of the instrumental records at different time-scales, and in particular at long ones (i.e. stability);
- include model reconstructions to fill data gaps and to complement observations when these suffer from large uncertainties;
- include physical constraints, such as the equality between the spectrally-integrated SSI, and the TSI, which is measured independently;
- additionally, exploit the high coherence of the SSI variability to exclude incoherent instrumental noise and thereby improve its signal-to-noise ratio. **This approach, which has already been explored by *Cessateur et al.* [2011] can be incorporated as an intermediate step of the composite building, before the records are averaged. Since, however, it entails a decrease of the uncertainty, the latter must be carefully reevaluated.**

We recently applied a similar approach to the TSI [*Dudok de Wit et al.*, 2017] and to the sunspot number. Both have challenges on their own. With the TSI, no contributions from solar proxies are allowed. With sunspot numbers, the absence of absolute scale requires an additional normalization step. Although the maximum likelihood framework, which we are using here,

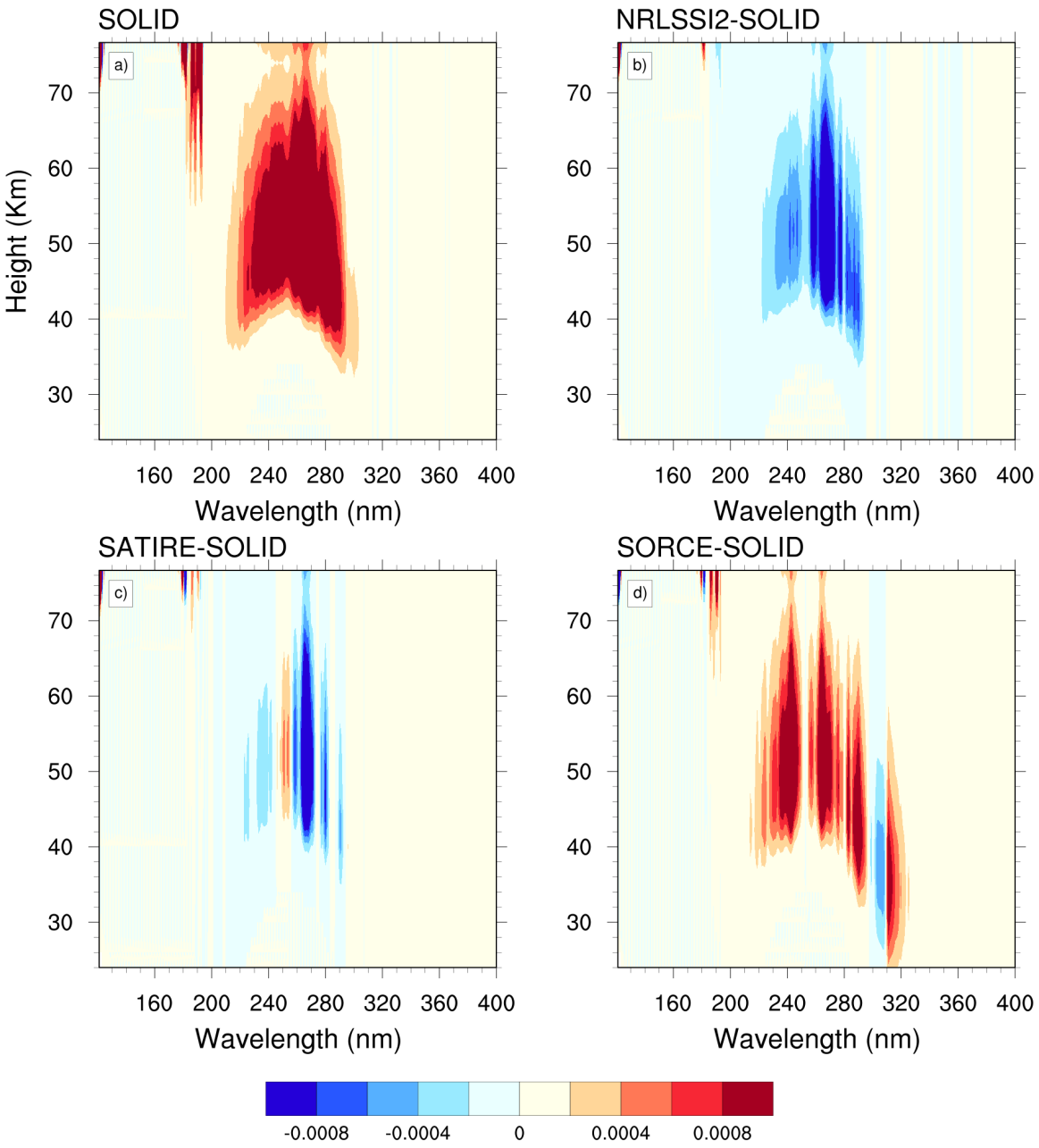

Figure 10. Panel a: Solar spectral heating rate anomalies (K/day/nm) between solar minimum (2008) and maximum (2003) for **the SOLID composite. The integral gives the total heating anomalies shown in Fig. 9a**. Panels b–d: Differences in the solar cycle heating rates **(K/day/nm)** between SOLID and NRLSSI2, SATIRE-S and SORCE, respectively.

is well suited for such purposes, eventually a Bayesian approach will be required to properly specify the prior information.

In order to understand the role of the Sun as one of the natural forcing mechanisms it is crucial to have a realistic estimate of the solar irradiance variability at hand. With the work presented we are confident we achieved a considerable step closer towards this goal.

Acknowledgments. The authors acknowledge that the research leading to these results has received funding from the European Community Seventh Framework Programme (FP7 2012) under grant agreement no 313188 (SOLID, http://projects.pmodwrc.ch/solid). Moreover, this work was supported by the COST Action ES1005 TOSCA (Towards a more complete assessment of the impact of solar variability on the Earths climate). This research has made use of NASA's Astrophysics Data System. We gratefully acknowledge all the instrumental teams for making their data freely available.

Notes

1. http://lasp.colorado.edu/lisird/sorce/sorce_ssi/index.html

2. http://homepages.see.leeds.ac.uk/ earpmf/ccmvalrad.shtml

References

Austin, J., et al. (2008), Coupled chemistry climate model simulations of the solar cycle in ozone and temperature, *Journal of Geophysical Research-Atmospheres*, *113*(D11), D11,306.

Bailey, S. M., T. N. Woods, C. A. Barth, S. C. Solomon, L. R. Canfield, and R. Korde (2000), Measurements of the solar soft X-ray irradiance by the Student Nitric Oxide Explorer: First analysis and underflight calibrations, J. Geophys. Res., *105*, 27,179–27,194, doi:10.1029/2000JA000188.

Ball, W. T., N. A. Krivova, Y. C. Unruh, J. D. Haigh, and S. K. Solanki (2014), A New SATIRE-S Spectral Solar Irradiance Reconstruction for Solar Cycles 21-23 and Its Implications for Stratospheric Ozone*, *Journal of Atmospheric Sciences*, *71*, 4086–4101, doi:10.1175/JAS-D-13-0241.1.

Ball, W. T., J. D. Haigh, E. V. Rozanov, A. Kuchar, T. Sukhodolov, F. Tummon, A. V. Shapiro, and W. Schmutz (2016), High solar cycle spectral variations inconsistent with stratospheric ozone observations, *Nature Geoscience*, *9*, 206–209, doi:10.1038/ngeo2640.

Brueckner, G. E., K. L. Edlow, L. E. Floyd, J. L. Lean, and M. E. Vanhoosier (1993), The solar ultraviolet spectral irradiance monitor (SUSIM) experiment on board the Upper Atmosphere Research Satellite (UARS), J. Geophys. Res., *98*, 10,695.

Cahalan, R. F., G. Wen, J. W. Harder, and P. Pilewskie (2010), Temperature responses to spectral solar variability on decadal time scales, *Geophys. Res. Lett.*, *37*, L07705, doi:10.1029/2009GL041898.

Cebula, R. P., M. T. DeLand, and E. Hilsenrath (1998), NOAA 11 solar backscattered ultraviolet, model 2 (SBUV/2) instrument solar spectral irradiance measurements in 1989-1994 1. Observations and long-term calibration, J. Geophys. Res., *103*, 16,235–16,250, doi:10.1029/98JD01205.

Cessateur, G., T. Dudok de Wit, M. Kretzschmar, J. Lilensten, and J.-F. Hochedez (2011), Monitoring the Solar UV Irradiance Spectrum from the Observation of a few Passbands, *Astronomy and Astrophysics*, *528*, A68, doi:10.1051/0004-6361/201015903.

Cessateur, G., et al. (2016), Solar irradiance observations with PREMOS filter radiometers on the PICARD mission: In-flight performance and data release, *Astronomy and Astrophysics*, *588*, A126, doi:10.1051/0004-6361/201527577.

Coddington, O., J. L. Lean, P. Pilewskie, M. Snow, and D. Lindholm (2016), A Solar Irradiance Climate Data Record, *Bulletin of the American Meteorological Society*, *97*, 1265, doi:BAMS-D-14-00265.1.

DeLand, M. T., and R. P. Cebula (2001), Spectral solar UV irradiance data for cycle 21, J. Geophys. Res., *106*, 21,569–21,584, doi:10.1029/2000JA000436.

DeLand, M. T., and R. P. Cebula (2008), Creation of a composite solar ultraviolet irradiance data set, *Journal of Geophysical Research (Space Physics)*, *113*, 11,103, doi:10.1029/2008JA013401.

Deland, M. T., and R. P. Cebula (2012), Solar UV variations during the decline of Cycle 23, *Journal of Atmospheric and Solar-Terrestrial Physics*, *77*, 225–234, doi:10.1016/j.jastp.2012.01.007.

DeLand, M. T., R. P. Cebula, and E. Hilsenrath (2004), Observations of solar spectral irradiance change during cycle 22 from NOAA-9 Solar Backscattered Ultraviolet Model 2 (SBUV/2), *Journal of Geophysical Research (Atmospheres)*, *109*, D06304, doi:10.1029/2003JD004074.

Donoho, D. L., and I. M. Johnstone (1995), Adapting to unknown smoothness via wavelet shrinkage, *Journal of the American Statistical Association*, *90*(432), 1200–1224, doi:10.1080/01621459.1995.10476626.

Dudok de Wit, T. (2011), A method for filling gaps in solar irradiance and solar proxy data, *Astronomy and Astrophysics*, *533*, A29, doi:10.1051/0004-6361/201117024.

Dudok de Wit, T., S. Bruinsma, and K. Shibasaki (2014), Synoptic radio observations as proxies for upper atmosphere modelling, *Journal of Space Weather and Space Climate*, *4*(26), A06, doi:10.1051/swsc/2014003.

Dudok de Wit, T., G. Kopp, C. Fröhlich, and M. Schöll (2017), Making a composite out of multiple observations: the new Total Solar Irradiance composite, *Geophys. Res. Lett.*, *accepted*, doi:10.1002/2016GL071866.

Emde, C., et al. (2016), The libradtran software package for radiative transfer calculations (version 2.0.1), *Geosci. Model Dev.*, *9*(5), 1647–1672, doi:10.5194/gmd-9-1647-2016.

Eparvier, F. G., D. Crotser, A. R. Jones, W. E. McClintock, M. Snow, and T. N. Woods (2009), The Extreme Ultraviolet Sensor (EUVS) for GOES-R, in *Society of Photo-Optical Instrumentation Engineers (SPIE) Conference Series*, *Society of Photo-Optical Instrumentation Engineers (SPIE) Conference Series*, vol. 7438, p. 4, doi:10.1117/12.826445.

Ermolli, I., et al. (2013), Recent variability of the solar spectral irradiance and its impact on climate modelling, *Atmospheric Chemistry & Physics*, *13*, 3945–3977, doi:10.5194/acp-13-3945-2013.

Evans, J. S., D. J. Strickland, W. K. Woo, D. R. McMullin, S. P. Plunkett, R. A. Viereck, S. M. Hill, T. N. Woods, and F. G. Eparvier (2010), Early Observations by the GOES-13 Solar Extreme Ultraviolet Sensor (EUVS), Sol. Phys., *262*, 71–115, doi:10.1007/s11207-009-9491-x.

Fontenla, J. M., P. C. Stancil, and E. Landi (2015), Solar Spectral Irradiance, Solar Activity, and the Near-Ultra-Violet, ApJ, *809*, 157, doi:10.1088/0004-637X/809/2/157.

Fröhlich, C., and J. Lean (1998), The Sun's total irradiance: Cycles, trends, and related climate change uncertainties since 1976, *Geophys. Res. Lett.*, *25*, 4377–4380.

Fröhlich, C., and J. Lean (2004), Solar radiative output and its variability: evidence and mechanisms, *Astron. Astroph. Review*, *12*, 273–320, doi:10.1007/s00159-004-0024-1.

Fröhlich, C., et al. (1995), VIRGO: Experiment for Helioseismology and Solar Irradiance Monitoring, Sol. Phys., *162*, 101–128, doi:10.1007/BF00733428.

Gray, L. J., S. T. Rumbold, and K. P. Shine (2009), Stratospheric temperature and radiative forcing response to 11-year solar cycle changes in irradiance and ozone, *Journal of the Atmospheric Sciences*, *66*(8), 2402–2417.

Gray, L. J., et al. (2010), Solar Influences on Climate, *Reviews of Geophysics*, *48*, RG4001, doi:10.1029/2009RG000282.

Haigh, J. D. (1994), The role of stratospheric ozone in modulating the solar radiative forcing of climate, *Nature*, *370*(6490), 544–546.

Haigh, J. D. (2007), The Sun and the Earth's Climate, *Living Reviews in Solar Physics*, *4*, doi:10.12942/lrsp-2007-2.

Haigh, J. D., A. R. Winning, R. Toumi, and J. W. Harder (2010), An influence of solar spectral variations on radiative forcing of climate, *Nature*, *467*, 696–699, doi:10.1038/nature09426.

Harrison, R. A., et al. (1995), The Coronal Diagnostic Spectrometer for the Solar and Heliospheric Observatory, *Solar Physics*, *162*, 233–290, doi:10.1007/BF00733431.

Hood, L., et al. (2015), Solar signals in cmip-5 simulations: The ozone response, *Quarterly Journal of the Royal Meteorological Society*, *141*, 26702689.

Kopp, G., and J. L. Lean (2011), A new, lower value of total solar irradiance: Evidence and climate significance, *Geophys. Res. Lett.*, *38*, L01706, doi:10.1029/2010GL045777.

Lean, J. (2000), Evolution of the Sun's Spectral Irradiance Since the Maunder Minimum, *Geophys. Res. Lett.*, *27*, 2425–2428, doi:10.1029/2000GL000043.

Lean, J. L., and M. T. DeLand (2012), How Does the Sun's Spectrum Vary?, *Journal of Climate*, *25*, 2555–2560, doi:10.1175/JCLI-D-11-00571.1.

Matthes, K., Y. Kuroda, K. Kodera, and U. Langematz (2006), Transfer of the solar signal from the stratosphere to the troposphere: Northern winter, *Journal of Geophysical Research-Atmospheres*, *111*(D6), D06,108, doi:10.1029/2005JD006283.

Meehl, G. A., J. M. Arblaster, K. Matthes, F. Sassi, and H. van Loon (2009), Amplifying the pacific climate system response to a small 11-year solar cycle forcing, *Science*, *325*(5944), 1114–1118, doi:10.1126/science.1172872.

Merkel, A. W., J. W. Harder, D. R. Marsh, A. K. Smith, J. M. Fontenla, and T. N. Woods (2011), The impact of solar spectral irradiance variability on middle atmospheric ozone, Geophys. Res. Lett., *38*, L13802, doi:10.1029/2011GL047561.

Misios, S., et al. (2015), Solar signals in cmip-5 simulations: Effects of atmospherre ocean coupling, *Quarterly Journal of the Royal Meteorological Society*.

Mitchell, D., et al. (2015), Solar signals in cmip-5 simulations: The stratospheric pathway, *Quarterly Journal of the Royal Meteorological Society*, *141*, 2390–2403.

Oberländer, S., et al. (2012), The influence of spectral solar irradiance data on stratospheric heating rates during the 11 year solar cycle, *Geophysical Research Letters*, *39*(1), L01,801, doi:10.1029/2011gl049539.

Rottman, G. (2005), The SORCE Mission, Sol. Phys., *230*, 7–25, doi:10.1007/s11207-005-8112-6.

Rottman, G., J. Harder, J. Fontenla, T. Woods, O. R. White, and G. M. Lawrence (2005), The Spectral Irradiance Monitor (SIM): Early Observations, Sol. Phys., *230*, 205–224, doi:10.1007/s11207-005-1530-7.

Rottman, G. J., C. A. Barth, R. J. Thomas, G. H. Mount, G. M. Lawrence, D. W. Rusch, R. W. Sanders, G. E. Thomas, and J. London (1982), Solar spectral irradiance, 120 to 190 nm, October 13, 1981 - January 3, 1982, *Geophys. Res. Lett.*, *9*, 587–590, doi:10.1029/GL009i005p00587.

Rottman, G. J., T. N. Woods, and T. P. Sparn (1993), Solar-Stellar Irradiance Comparison Experiment 1. I - Instrument design and operation, J. Geophys. Res., *98*, 10,667, doi:10.1029/93JD00462.

Schmidtke, G., B. Nikutowski, C. Jacobi, R. Brunner, C. Erhardt, S. Knecht, J. Scherle, and J. Schlagenhauf (2014), Solar EUV Irradiance Measurements by the Auto-Calibrating EUV Spectrometers (SolACES) Aboard the International Space Station (ISS), Sol. Phys., *289*, 1863–1883, doi:10.1007/s11207-013-0430-5.

Schmutz, W., et al. (2009), The PREMOS/PICARD instrument calibration, *Metrologia*, *46*, 202–206, doi:10.1088/0026-1394/46/4/S13.

Schöll, M., T. Dudok de Wit, M. Kretzschmar, and M. Haberreiter (2016), Making of a solar spectral irradiance dataset I: observations, uncertainties, and methods, *Journal of Space Weather and Space Climate*, *6*(27), A14, doi:10.1051/swsc/2016007.

Skupin, J., M. Weber, S. Noël, H. Bovensmann, and J. P. Burrows (2005), GOME and SCIAMACHY solar measurements: Solar spectral irradiance and Mg II solar activity proxy indicator, Mem. Soc. Astron. Italiana, *76*, 1038.

Solanki, S. K., N. A. Krivova, and J. D. Haigh (2013), Solar Irradiance Variability and Climate, ARA&A, *51*, 311–351, doi:10.1146/annurev-astro-082812-141007.

Starck, J.-L., F. Murtagh, and J. M. Fadili (2010), *Sparse image and signal processing: wavelets, curvelets, morphological diversity*, Cambridge University Press, Cambridge.

Stocker, T., and D. Qin (Eds.) (2014), *Climate Change 2013 - The Physical Science Basis. Working Group I Contribution to the Fifth Assessment Report of the IPCC.*, Cambridge University Press, Cambridge.

Swartz, W. H., R. S. Stolarski, L. D. Oman, E. L. Fleming, and C. H. Jackman (2012), Middle atmosphere response to different descriptions of the 11-yr solar cycle in spectral irradiance in a chemistry-climate model, *Atmospheric Chemistry & Physics*, *12*, 5937–5948, doi:10.5194/acp-12-5937-2012.

Thuillier, G., L. Floyd, T. N. Woods, R. Cebula, E. Hilsenrath, M. Hersé, and D. Labs (2004), Solar irradiance reference spectra for two solar active levels, *Advances in Space Research*, *34*, 256–261, doi:10.1016/j.asr.2002.12.004.

Thuillier, G., S. Dewitte, W. Schmutz, and Picard Team (2006), Simultaneous measurement of the total solar irradiance and solar diameter by the PICARD mission, *Advances in Space Research*, *38*, 1792–1806, doi:10.1016/j.asr.2006.04.034.

Viereck, R., L. Puga, D. McMullin, D. Judge, M. Weber, and W. K. Tobiska (2001), The Mg II index: A proxy for solar EUV, *Geophysical Research Letters*, *28*, 1343–1346, doi:10.1029/2000GL012551.

Wehrli, C., W. Schmutz, and A. I. Shapiro (2013), Correlation of spectral solar irradiance with solar activity as measured by VIRGO, A&A, *556*, L3, doi:10.1051/0004-6361/201220864.

Wieman, S. R., L. V. Didkovsky, and D. L. Judge (2014), Resolving Differences in Absolute Irradiance Measurements Between the SOHO/CELIAS/SEM and the SDO/EVE, *Solar Physics*, *289*, 2907–2925, doi:10.1007/s11207-014-0519-5.

Wilson, R. M., and D. H. Hathaway (2006), On the Relation Between Sunspot Area and Sunspot Number, *NASA STI/Recon Technical Report N*, *6*, 20,186.

Woods, T. N., and G. Rottman (2005), XUV Photometer System (XPS): Solar Variations during the SORCE Mission, Sol. Phys., *230*, 375–387, doi:10.1007/s11207-005-2555-7.

Woods, T. N., G. J. Rottman, R. G. Roble, O. R. White, S. C. Solomon, G. M. Lawrence, J. Lean, and W. K. Tobiska (1994), Thermosphere-Ionsphere-Mesosphere Energetics and Dynamics (TIMED) Solar EUV Experiment, in *Optical Spectroscopic Techniques and Instrumentation for Atmospheric and Space Research*, *Society of Photo-Optical Instrumentation Engineers (SPIE) Conference Series*, vol. 2266, edited by J. Wang and P. B. Hays, pp. 467–478.

Woods, T. N., E. M. Rodgers, S. M. Bailey, F. G. Eparvier, and G. J. Ucker (1999), TIMED solar EUV experiment: preflight calibration results for the XUV photometer system, in *Optical Spectroscopic Techniques and Instrumentation for Atmospheric and Space Research III*, *Society of Photo-Optical Instrumentation Engineers (SPIE) Conference Series*, vol. 3756, edited by A. M. Larar, pp. 255–264.

Woods, T. N., W. K. Tobiska, G. J. Rottman, and J. R. Worden (2000), Improved solar Lyman α irradiance modeling from 1947 through 1999 based on UARS observations, J. Geophys. Res., *105*, 27,195–27,216, doi:10.1029/2000JA000051.

Woods, T. N., et al. (2012), Extreme Ultraviolet Variability Experiment (EVE) on the Solar Dynamics Observatory (SDO): Overview of Science Objectives, Instrument Design, Data Products, and Model Developments, *Solar Physics*, *275*, 115–143, doi:10.1007/s11207-009-9487-6.

Yeo, K. L., N. A. Krivova, S. K. Solanki, and K. H. Glassmeier (2014), Reconstruction of total and spectral solar irradiance from 1974 to 2013 based on KPVT, SoHO/MDI, and SDO/HMI observations, A&A, *570*, A85, doi:10.1051/0004-6361/201423628.